Microfabricated Air-Microfluidic Sensor for Personal Monitoring of Airborne Particulate Matter: Design, Fabrication, and Experimental Results

Igor Paprotny[a,b,*], Frederik Doering[a], Paul A. Solomon[c], Richard M. White[a], Lara Gundel[b]

[a] *Berkeley Sensor and Actuator Center, University of California, Berkeley, CA, USA.*
[b] *Environmental Energy Technologies Division, Lawrence Berkeley National Laboratory, Berkeley, CA, USA.*
[c] *Office of Research and Development, Environmental Protection Agency, Las Vegas, NV, USA.*

Abstract

We present the design and fabrication of a micro electro mechanical systems (MEMS) air-microfluidic particulate matter (PM) sensor, and show experimental results obtained from exposing the sensor to concentrations of tobacco smoke and diesel exhaust, two commonly occurring PM sources. Our sensor measures only 25 mm × 21 mm × 2 mm in size and is two orders of magnitude smaller than commercially available direct mass PM sensors. The small shape allows our sensor to be used for continuous recording of personal PM exposure levels. The sensor contains an air-microfluidic circuit that separates the particles by size (virtual impactor) and then transports and deposits the selected particles using thermophoretic precipitation onto the surface of a microfabricated mass-sensitive film bulk acoustic resonator (FBAR). The mass-loading of the FBAR causes a change in its resonant frequency, and the rate of the frequency change corresponds to the particle concentration in the sampled air-volume. We present experimental results that demonstrate the performance of our sensor for measuring PM-mass emitted from diesel exhaust and tobacco smoke, and show that it exhibits low-end sensitivity on

*Corresponding author
Email addresses: igorpapa@eecs.berkeley.edu (Igor Paprotny), Solomon.Paul@epamail.epa.gov (Paul A. Solomon), rwhite@eecs.berkeley.edu (Richard M. White), LAGundel@lbl.gov (Lara Gundel)

the order of 2 $\mu g/m^3$ with up to 10 min integration time.

Keywords:
air quality monitoring, $PM_{2.5}$, air-microfluidics, MEMS

1. Introduction

Atmospheric particulate matter (PM) is a category of airborne pollutants that include dust, tobacco smoke, diesel exhaust, and other primary sources and secondary particles formed from gas phase precursors. Fine particles that have a diameter of 2.5 microns or smaller ($PM_{2.5}$) are especially damaging to human health because of their ability to penetrate deep into our respiratory system [1]. Exposure to $PM_{2.5}$ has been linked to reduced lung functionality, bronchitis, and heart attacks [2, 3, 4]. The negative health impacts of $PM_{2.5}$ have, for example, recently prompted the U.S. Environmental Protection Agency (EPA) to formulate new rules for the safe exposure limits of $PM_{2.5}$ [5] and influenced the Beijing Municipal Environmental Protection Bureau to start publishing $PM_{2.5}$ levels in response to high public demand. While the increasing awareness of the negative health impacts of PM shows the need for higher spatial density monitoring, the currently available direct mass PM sensors lack the form factor that will allow seamless integration into a device that can perform continuous personal monitoring of $PM_{2.5}$ exposure levels. Although light-scattering based PM sensors such as [6, 7] have been made portable, such sensors collect particle count data and have to infer the particle concentration based on assumptions regarding particle density and size distribution, reducing their accuracy and applicability.

In this work we present the design and fabrication of a MEMS air-microfluidic particulate matter (PM) sensor, and show experimental results obtained by exposing the sensor to concentrations of tobacco smoke and diesel exhaust, two commonly occurring PM sources. Our sensor is two orders of magnitude smaller than commercially available PM mass sensors, and is an order of magnitude smaller than the prototype previously developed in our lab [8]. Its small size (25 mm $\times$ 21 mm $\times$ 2 mm) enables easy integration into a portable platform for personal $PM_{2.5}$ monitoring. The sensor consists of an microfabricated air-microfluidic circuit that provides both filtration for the target particle size (virtual impactation) and direct measurement of the particle mass concentration using a mass-sensing microelectromechanical film bulk acoustic resonator (FBAR). In this paper, we describe the the design

of the sensor, provide a detailed description of its microfabrication process, and present the experimental results obtained form exposing two fabricated sensor prototypes to tobacco smoke and diesel exhaust. The results show that our sensor has low-end sensitivity on the order of 2 $\mu g/m^3$, which is adequate for personal pollution monitoring applications. An abbreviated version of this work was previously presented in [9].

The remainder of the paper is structured as follows: In Section 2 we briefly describe the related work regarding small-sized PM sensors. A description of the principles of operation of our sensor and the design of the air-microfluidic circuit is presented in Section 3. The microfabrication process of the three-wafer stack constituting the PM sensor is described in detail in Section 4. Section 5 describes the experimental setup, while Section 6 describes the experimental results, detailing the exposure of our sensor to both tobacco smoke and diesel exhaust. Finally, Section 7 concludes with a discussion of the applications of the presented technology to personalized monitoring of PM exposure levels and discusses future work.

2. Related Work

PM concentration is determined by either measuring PM mass in a given size range by gravimetry or estimating it from an indirect measurement such as light scattering [10, 11]. Direct gravimetric methods are either time-integrated, that is, particles are collected on a filter and weighed in a laboratory after collection [12] or continuously (1-hr average or less), where particles are collected on a sensing element, such as a tapered element oscillating microbalance (TEOM) [13] or a quartz-crystal microbalance (QCM) [13]. Mass is measured in the latter two based on the change in frequency of the oscillating element or piezoelectric resonator, respectively. The most common indirect method for estimating PM mass over the size range of 0.3 to 10 μm in diameter is based on light scattering [11, 13]. In this case, particles are illuminated by single or multiple wavelengths of light and the scattered light (forward and or backscattered) is measured and can provide an estimate of the mass of particles in a given volume of air. A number of assumptions are made in this indirect measurement of PM mass [11].

Particles within a given size range are most often obtained based on particle inertia. Widely used approaches include impactors, cyclones, and virtual impactors [14]. In all three cases particles are accelerated through a jet (e.g., nozzle or slit) to obtain a certain inertia. Particles smaller than the

desired cutpoint follow a major air flow, while those greater than the desired cutpoint are removed either by a real surface (plate or wall, the latter in the case of a cyclone) or through a minor flow collection jet (nozzle) in the case of the virtual impactor. Recently, miniature virtual impactors, cyclones, and real-impactors have been developed to separate particles at very low flow rates, in the range of 0.005 to 0.5 L/min [15, 16, 17].

Personal PM monitoring relies on portable mini-samplers that can be unobtrusively carried by individuals to record their PM exposure as they go about their daily activities [18]. Currently, these devices operate at flow rates of few L/min, weigh up to a kg, and be more than 10 cm in height [19, 20, 21]. In contrast, the device presented in this work measures 25 mm $\times$ 21 mm $\times$ 2 mm, weighs only a few grams, and operates at a flow-rate of approximately 6 mL/min. This low flow-rate enables low-power operation which further accommodates a portable personal PM monitor application. A good comparison of this and other small-scale sensors is presented in [22].

3. System Design

Figure 1 shows a schematic drawing illustrating the functionality of our air-microfluidic micro electro mechanical systems (MEMS) PM sensor. Air enters the microfluidic circuit through the inlet and immediately flows into an inertial size separator, commonly known as a *virtual impactor* (VI) [14] (a). The VI separates particles by size into a fine particle stream containing particles with mean aerodynamic diameter (AD) less than 2.5 μm, and a coarse particle stream, which contains particles that are larger than 2.5 μm mean AD. Our sensor is designed to measure the concentrations of fine particles only, and thus the coarse particle stream is simply exhausted through the outlet. Fine particles are then directed to the thermophoretic deposition region (b) where a temperature gradient induced across the microfluidic channel removes particles from the airstream by *thermophoresis*. The particles removed from the airstream are deposited on the exposed surface of a mass-sensing FBAR (c). The rate of particle deposition, corresponding to the rate of change in the resonant frequency of the FBAR is proportional to the concentration of the particles in the airstream. This rate of change is recorded using electronic down-converter circuitry (d) and converted to a format that can be stamped with GPS-based time and location information for subsequent transmission through a cellular radio (e) to an off-board central

repository [22]. In this work, (d) was replaced with a computer-controlled spectrum analyzer, while (e) was left for future work.

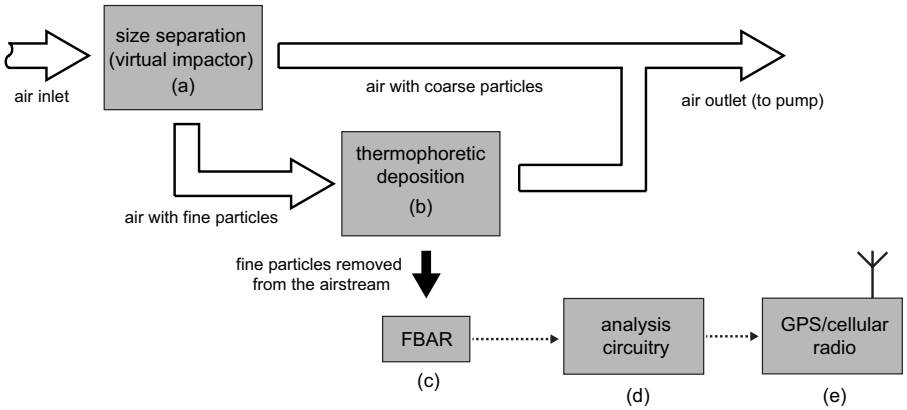

Figure 1: Schematic drawing illustrating the components and functionality of the air-microfluidic MEMS PM sensor.

The design of the microfluidic circuit is shown in Figure 2. The entire circuit occupies an area of approximately 5 cm^2. Negative pressure that drives the air from the inlet to the outlet is provided by a pump composed of a stack of commercially available miniature fans (15 mm $\times$ 15 mm $\times$ 10 mm).

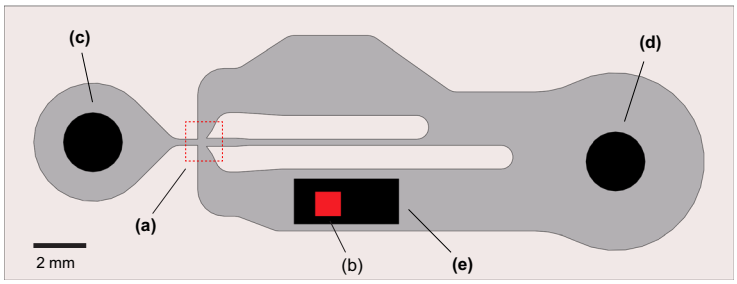

Figure 2: Layout design of the microfluidic circuit. The VI and the thermophoretic deposition region are annotated (a) and (b), respectively. The dark gray areas indicate the flow channels of the microfluidic circuit, while the black regions indicate the through-holes for the inlet (c), outlet (d), and the FBAR insertion opening (e).

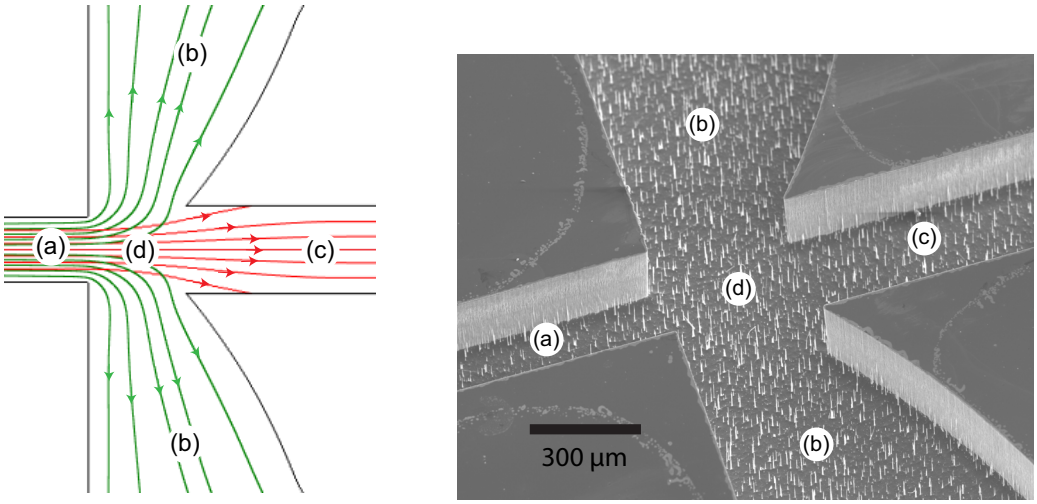

Figure 3: Microfabricated virtual impactor (VI): **(left)** Particle traces (obtained using the FEM) for particle diameters 1 μm (green) and 5 μm (red) that originate in the acceleration jet (a) and end up in the major (b) and minor (c) flows, respectively. Label (d) refers to the jet spacing. **(right)** Scanning-electron micrograph (SEM) of the microfabricated channels of the VI.

3.1. Particle Size Selection (Virtual Impactor)

PM initially enters the microfabricated VI to ensure that particles with larger than 2.5 μm AD (50% collection efficiency) are removed from the flow. Figure 3 shows the operation of the VI obtained using the finite element method (FEM) (left) and an SEM image for the microfabricated structure (right). The majority of the air from the acceleration jet (a) is diverted into the major flow channels (b) of the VI. Large particles with greater inertia cross the gap (d) into the minor flow channel (c).

The ratio of particles that follow the major flow stream (b) to the total number of particles that enter the inlet increases with decreasing particle size. The 50% collection efficiency, the point where this ratio is equal to 0.5, is defined as the *cutpoint* of the VI. From [14] the cutpoint can be approximated as

$$d_{50} = \sqrt{\frac{9\eta W^2 D(Stk_{50})}{\rho_p Q C_c}}, \tag{1}$$

where η is the dynamic viscosity of air, W and D are the width and depth of the impactor jet respectively, ρ_p is the particle density, Q is the volumet-

ric flowrate through the inlet jet, and Stk_{50} is the stokes number, which is recommended to be 0.59 for rectangular jet impactors. The Cunningham correction factor for particles larger than 1 μm C_c is defined as

$$C_c = 1 + \frac{2.52\lambda}{d}, \tag{2}$$

where d is the particle diameter and λ is the length of the mean free path of air.

The microfabricated VI design was further adjusted using FEM to obtain a 2.5 μm particle cutpoint at the flow rate of 6 mL/min. Figure 4 shows the fine particle *collection efficiency* curve of the VI (the ratio of particles that follow the major flow relative to the number of particles that enter the inlet as a function of their diameter). The FEM was implemented using COMSOL [23] and its particle tracing algorithm with particles uniformly distributed in a steady-state three dimensional flow field.

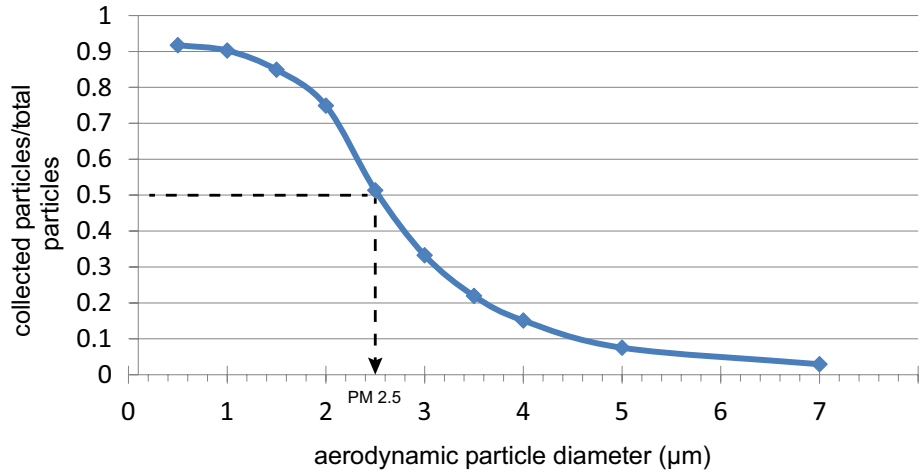

Figure 4: Fine particle collection efficiency curve of the microfabricated VI at 6 mL/min. obtained using the FEM.

The small size of the microfabricated VI allows our sensor to operate at a low flow rate (6 mL/min), which in turns helps to reduce the power consumption of the outlet pump. For ease of fabrication, a rectangular channel cross section was used. The air flows in the minor and major flow channels were balanced by adjusting the cross-section areas of the two flow channels

(see Figure 2) affecting the viscous pressure drop and the resulting flow rate, and allowing only one air inlet and outlet to be used.

3.2. Thermophoretic Particle Deposition

Once the coarse (> 2.5 μm AD) particles have been removed through the coarse particle channel of the VI, half of the remaining $PM_{2.5}$ stream proceed to the mass sensing area, where a fraction of the particles is removed from the flow and deposited on the surface of a mass-sensing FBAR using thermophoresis. Microfabricated heaters suspended above the mass-sensing FBAR create a temperature gradient across the microfluidic channel. The air molecules on the hotter side of each particle transfer slightly more momentum to the particle than the molecules on its cooler side, creating a thermophoretic force F_{th} in the direction of the temperature gradient. Based on [14] F_{th} can be approximated as

$$F_{th} = -\frac{9\pi d\eta^2 H(\delta T)}{2\rho_g T}, \tag{3}$$

where δT is the temperature gradient, T is the absolute temperature of the air, and H is the molecular accommodation coefficient, which using the molecular accommodation coefficient suggested by [24], is defined as

$$H \cong \left(\frac{1}{1+6\lambda/d}\right)\left(\frac{k_a/k_p + 4.4\lambda/d}{1+2k_a/k_p + 8.8\lambda/d}\right), \tag{4}$$

where k_a and k_p are thermal conductivities of air and particles, respectively. The absolute temperature T can be approximated as the average of the absolute temperatures of the heater and the FBAR surface. Equating F_{th} with the Stokes drag force yields a thermophoretic particle velocity V_{th} [14] defined as

$$V_{th} = \frac{-3\eta C_c H(\delta T)}{2\rho_g T}, \tag{5}$$

In our design, the deposition thermal velocity was calculated to be approximately 1.36 mm/s, with a temperature gradient δT of 1×10^6 K/m. The temperature gradient is generated by the microfabricated heaters above the FBAR, and is a function of the applied heater power on the hot side, and a combination of convective and conductive cooling on the cold side. The airstream passing between the heater and the FBAR absorbs most of

the heat, while the rest is dissipated to the environment by conduction. To minimize heat loss to the environment, and hence reduce heat consumption, the capping wafer that serves as the heater substrate was designed using quartz, taking advantage of its low thermal conductivity (1.3 W/K/m). As we describe in Section 4 below, the heaters were suspended below the capping quartz wafer to further limit the heat losses.

3.3. Particle Mass Sensing

Particles are deposited on to the surface of the FBAR as the result of applied thermophoretic force. Under constant δT the rate of deposition is proportional to the concentration of the particles in the sampled air. An FBAR consists of a piezoelectric layer sandwiched between bottom and top electrodes and suspended over an airgap to ensure maximum reflection of the acoustic energy, as illustrated in the cross-section drawing of the FBAR shown in Figure 5.

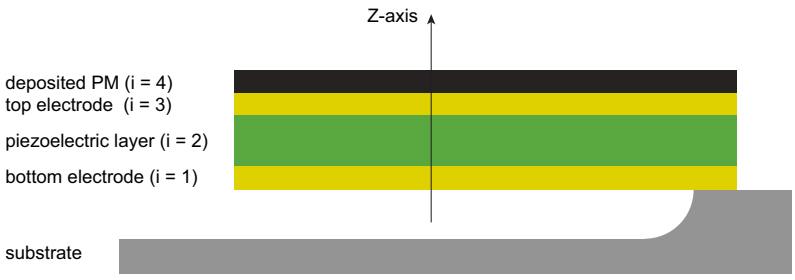

Figure 5: Cross-section showing the individual layers of the mass-sensing FBAR. Acoustically active (i = 2) and passive (i = 1,3,4) layers are shown. The Z-axis represents the direction of the dimension of the cross section used to develop the equivalent one-dimensional lump-parameter model.

Assuming a simplified one-dimensional electromechanical model along the z-direction (3^{rd} axis), the acoustic impedance Z_i of each layer i is defined [25] as

$$Z_i = \sqrt{\rho_i \overline{c}_{i,33}}, \tag{6}$$

where ρ_i is the density of the material in layer i, while $\overline{c}_{i,33}$ is defined as

$$\overline{c}_{i,33} = c_{i,33} + j\omega\eta_i, \tag{7}$$

where $c_{i,33}$ is the 33-mode short circuit stiffness and η_i is the material viscosity. The admittance of the FBAR can now be modeled using a lumped-parameter equivalent circuit for each layer and connecting them in series using the transmission-line model [26, 25]. The transmission line models for non-piezoelectric layers (i = 1,3,4), and the piezoelectric layer (i = 2), are shown in Figure 6. Stresses S_1 and S_2 and velocities v_1 and v_2 are the across and through variables, equivalent to voltage and current [27], in the mechanical domain, while V and I are voltage and currents in the electrical domain. $\mathbf{A}$ is the resonator area, t_i is the thickness of each layer, and k_i is the wave number defined as

$$k_i = \frac{\omega}{\sqrt{\frac{\bar{c}_{i,33}}{\rho_i}}}. \tag{8}$$

The turn ratio Γ is defined as

$$\Gamma = \frac{e_{33}}{\epsilon_{33}} C_0, \tag{9}$$

where e_{33} is the piezoelectric constant and ϵ_{33} is the dielectric constant, both in 33-mode, and C_0 is the clamped capacitance of the piezoelectric layer.

Assuming an operating point near resonance, the electric port impedance of the FBAR can be modeled as an RLC circuit in parallel with C_0. The FBAR is connected to a driver CMOS circuit as a Pierce oscillator [28]. The general topology for the circuit is shown on Figure 7a. The Pierce oscillator is used to generate reliable clock signals in many of today's consumer electronics. The feedback for the oscillation is formed through an inverting amplifier (M_1). The FBAR together with capacitors C_1 and C_2 provide a 180° phase shift (at the FBAR's resonant frequency). This results in an unstable positive feedback across M_3, which leads to circuit oscillation at the FBAR's resonant frequency [29]. The circuit was implemented using a foundry 0.25 μm complementary metal oxide semiconductor (CMOS) process with C_2 = 680 fF, C_1 = 99 fF [25]. An optical micrograph of a CMOS driver die is shown in Figure 7b. Visible are the bond wires used to connect the CMOS driver circuit to the FBAR. The close proximity of the CMOS driver circuit to the FBAR reduces the parasitics associated with long connecting wires, enabling proper functionality of the oscillator and reducing the noise. The output of the CMOS is a sinusoidal signal that oscillates at the resonant frequency of the FBAR.

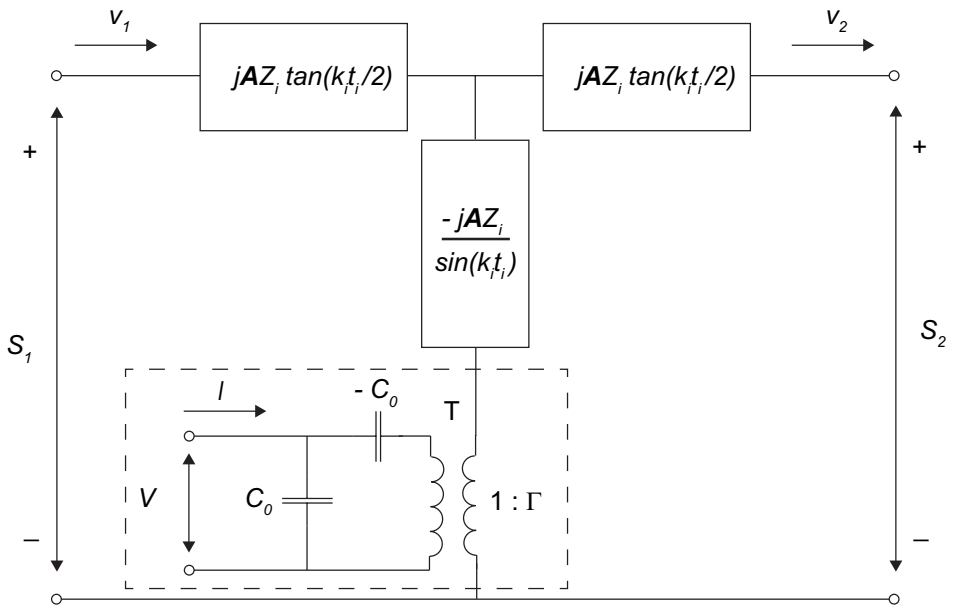

Figure 6: Transmission line lumped-parameter equivalent circuit of the individual layers of the FBAR. The transformer T and the corresponding electrical domain (enclosed by the dashed line) only applies to the piezoelectric layer ($i = 2$). T is removed and the resulting gap shorted when modeling the non-piezoelectric layers (i = 1,3,4).

For the purpose of this work, we assume a resonant frequency change proportional to the added particle mass, neglecting non-linear and higher order effects. Consequently, the *rate of change* of the resonant frequency of the oscillator (during constant thermophoretic deposition) is proportional to the particle concentration in the sampled air. The interested reader is referred to [25] for further detailed modeling of the FBAR performance during mass deposition.

4. Fabrication

An exploded CAD drawing of the air-microfluidic MEMS PM sensor is shown in Figure 8. The sensor is composed of three bonded wafers. The top wafer consists of fused quartz and serves as a transparent cap for the air-microfluidic channels, as well as the substrate for the thermophoretic heaters (a). The middle silicon wafer contains the etched air-microfluidic channels, the through-wafer opening for the air inlet (b) and outlet (c), as well as

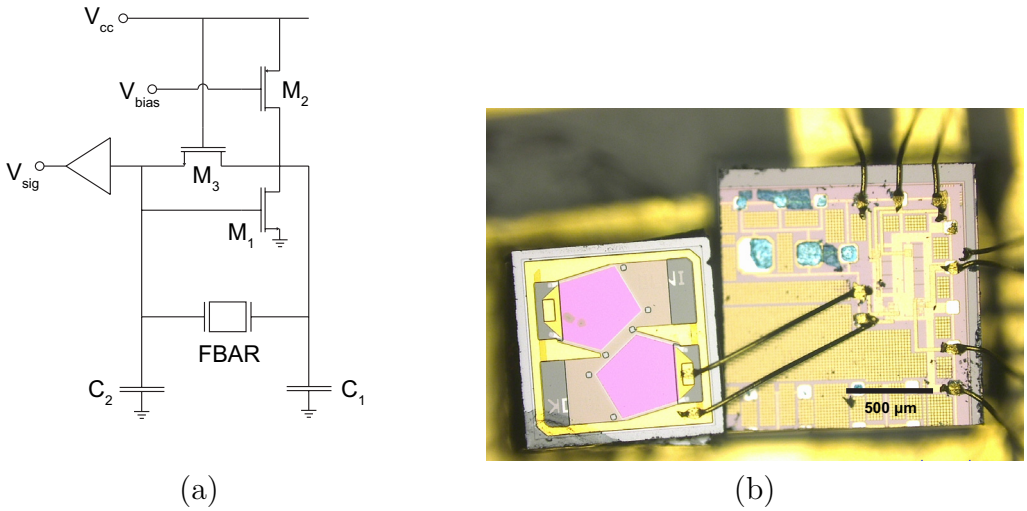

(a) (b)

Figure 7: Pierce oscillator CMOS circuit: **(a)** The schematic of the Pierce Oscillator circuit containing the FBAR, and **(b)** an optical micrograph of the CMOS driver circuit (right) connected to the FBAR (left). Bond wires, connecting the CMOS circuit to the leads on the bottom wafer are visible.

the rectangular opening (d) though which the FBAR is inserted into the microfluidic channel. The bottom fused quartz wafer contains the FBAR (e) and the CMOS driver (f) die, as well as the polymeric seal (g), which both seals the FBAR insertion opening and determines the depth of FBAR penetration into the microfluidic channel.

4.1. Thermophoretic Heaters (Top Wafer)

The fabrication process for the thermophoretic heaters is illustrated in Figure 9. First, a 2 μm thick layer of in-situ doped polysilicon is deposited through a low-pressure chemical vapour deposition (LPCVD) process (50 % SiH_4, 50 % PH_3, 615° C) on a fused quartz substrate. To avoid cracking the quartz wafer due to devitrification of its surface layer, the polysilicon layer is *not* annealed. However, the un-annealed polysilicon layer has a sheet resistance of $\approx$ 40 $\Omega/\square$, which, although significantly higher than typical sheet resistance of annealed in-situ doped polysilicon, is sufficiently low to produce the desired heating power at a manageable voltage. A 100 nm thick layer of gold (Au) with a 5 nm chrome adhesion layer (Cr) is evaporated on top of the polysilicon layer. The Cr/Au layer is then lithographically patterned

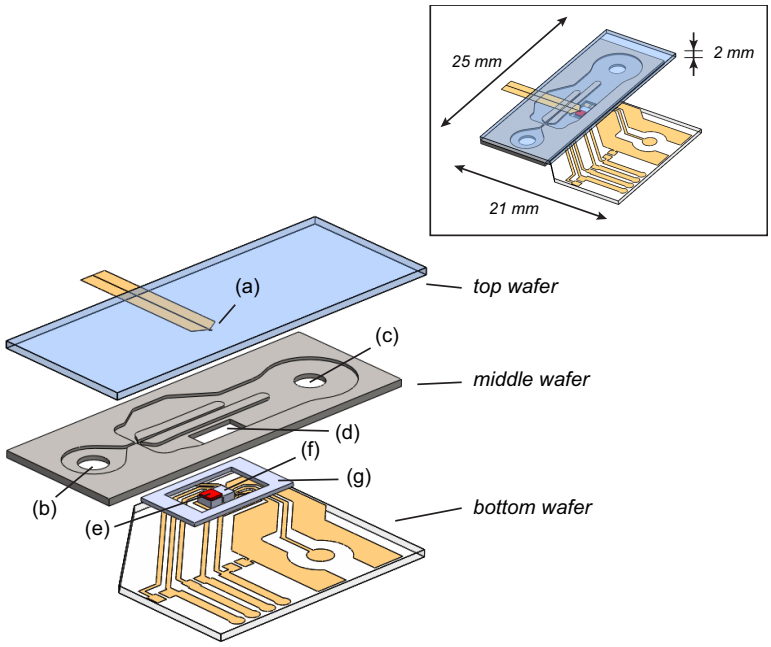

Figure 8: Exploded CAD drawing of the three-wafer stacked MEMS PM sensor. The inset shows a CAD drawing of the assembled sensor.

using an iodine-based gold etchant and CR-7, fabricating the high conductivity connections to the thermophoretic heaters. The polysilicon layer is then etched by a reactive ion-etch (RIE) process (90 % SF_6, 10 % O_2, 66 sccm) to create the resistive heater elements. The wafer is subsequently diced, and the individual die are soaked for 10 min in 49 % HF to release the heaters from the substrate. Optical micrographs of two fabricated thermophoretic heater designs, taken through the top quartz wafer are shown in Figure 10. The dark blue area (a) represents the under-etched quartz under the polysilicon layer. The resistance of the heaters was approximately 650 Ω and 8 kΩ for designs A and B, respectively.

4.2. Microfluidic Channels (Middle Wafer)

The fabrication process of the air-microfluidic channels in the middle wafer is illustrated in Figure 11. Starting with a p-type silicon wafer as the substrate, the microfluidic channels are lithographically patterned and etched to a depth of 200 μm using a deep reactive ion etch (DRIE) process (90% SF_6,10% O_2 RIE etch, C_4F_8 passivation). A backside DRIE etch is subse-

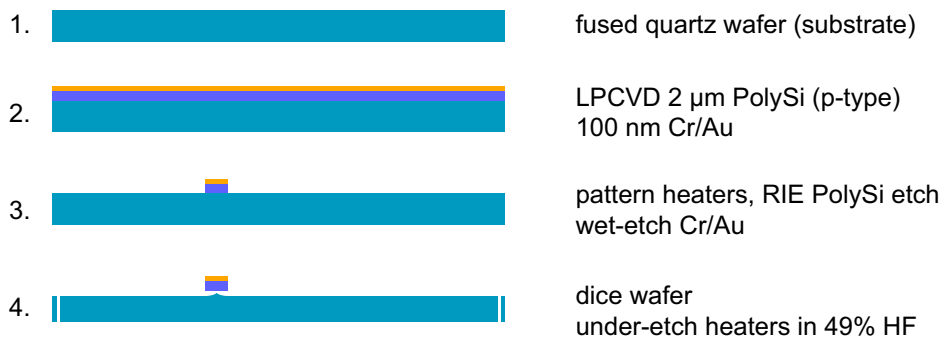

Figure 9: Fabrication process for the top wafer with attached thermophoretic heaters.

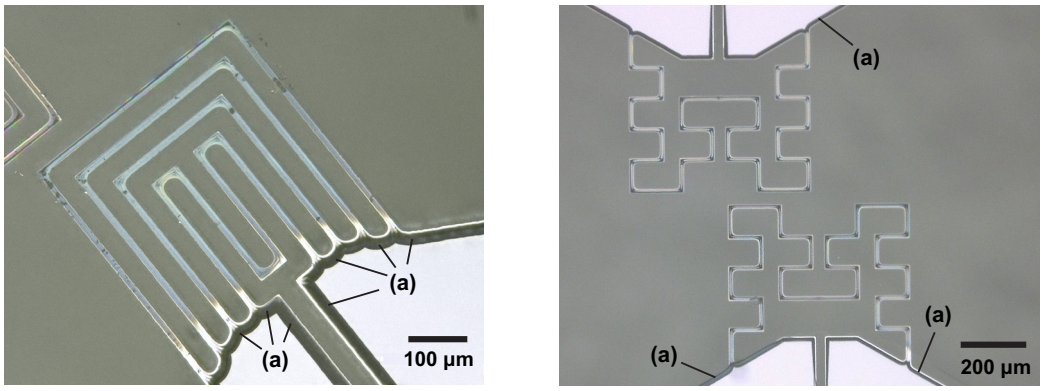

(a) (b)

Figure 10: Optical micrographs of the two types of fabricated and released thermophoretic heaters (design A (a) and design B (b)) obtained though the top quartz wafer. The rounding of the heaters' features is a byproduct of the fabrication process.

quently performed to open the inlet, outlet, and FBAR insertion opening. The wafer is subsequently diced into individual die.

4.3. FBAR and Circuitry Substrate (Bottom Wafer)

The fabrication process for the bottom wafer is illustrated in Figure 12. First, 5 nm/100 nm of Cr/Au is evaporated onto the wafer and lithographically patterned to form the power and signal thin-film traces that provide connections to the CMOS driver. The wafer is then diced. A 475 μm tall 1 mm $\times$ 1 mm pedestal is attached at the desired location of the FBAR using cyanoacrylate adhesive. The FBAR die is then bonded on top of the

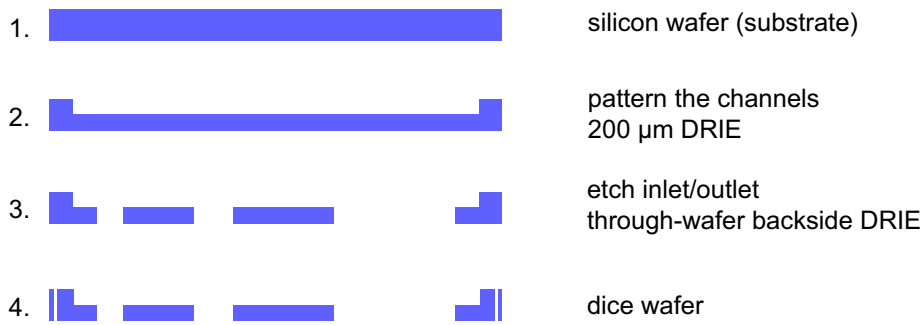

Figure 11: Fabrication process for the middle wafer containing the air-microfluidic channels.

pedestal, while the CMOS die is bonded next to the pedestal, again using the cyanoacrylate adhesive. The FBAR is wirebonded to the CMOS die, and then the CMOS die is wirebonded to the Cr/Au traces (See Figure 7b). Power and signal leads are subsequently soldered onto the Cr/Au traces. Finally, a 285 μm adhesive polymeric seal (made out of a triple stack of dicing tape) is attached, surrounding the FBAR and CMOS to provide a seal for the insertion opening, as well as, together with the pedestal, to set the distance the FBAR penetrates into the microfluidic channel. Although the seal is attached manually, its precise thickness is able to ensure the insertion of the FBAR with an accuracy of few tens of μm.

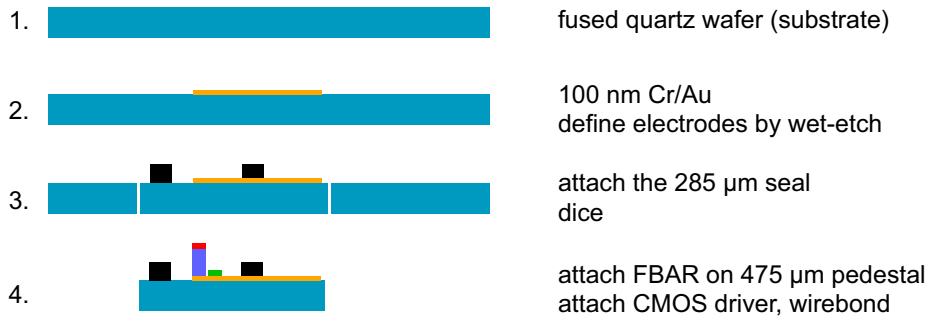

Figure 12: Fabrication process for the bottom wafer, which contains the mass-sensing FBAR and the CMOS driver.

4.4. Final Assembly

The top, middle, and bottom wafers are bonded together to form the final device. This bonding process is illustrated on Figure 13. First, a die from the top wafer is bonded with the matching die from the middle wafer. To make sure a good seal is achieved, especially around the small features of the microfluidic channel, we use adhesive bonding by applying dispenser-printed [30] epoxy (72% Epon 830 resin, 28% Epicure 3370 curing agent). The epoxy is printed to provide a seal around the perimeter of the microfluidic circuit as well as around the minor flow channel. The top wafer die is then aligned with the microfluidic circuit of the middle wafer die, and the two are pressed together and left overnight to cure on a 60° C hotplate. The same epoxy mixture is applied to the polymeric seal, and the bottom wafer is visually aligned and attached to the bonded top and middle wafers. The FBAR should now protrude into the microfluidic channel with a separation of approximately 100 μm from the surface of the thermophoretic heater. The sensor is finally sealed with silicone (Osi Sealant/Henkel Adhesive) around the edges of the bonded die to prevent leaks and increase the structural stability of the device.

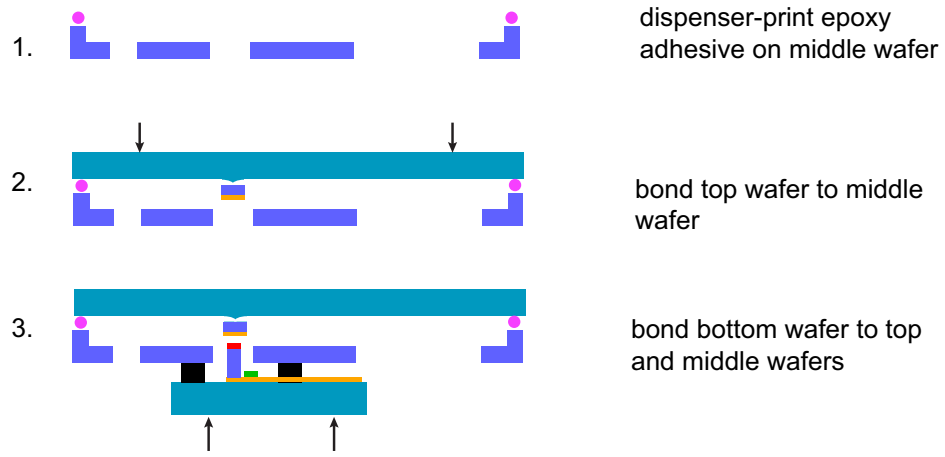

Figure 13: Final assembly of the top, middle, and bottom wafers to complete the fabrication of the MEMS PM sensor.

A fabricated sensor prototype is shown in Figure 14. The VI and thermophoretic regions are labeled (a) and (b), respectively. Also visible through the top quartz wafer are traces of the dispenser, printed epoxy (c). The

alignment of the three layers can be seen in the optical micrograph shown in Figure 15. The two FBARs are visible as pink pentagons, partially obscured by the thermophoretic heaters above them. Only one (bottom) FBAR was intended for PM sensing, and only this FBAR is properly aligned with the above heater. The brown discoloration visible around the outlet hole are under-etched silicon spires commonly called silicon grass. Silicon grass is a by-product of the DRIE fabrication process, and is mostly downstream of the mass-sensing FBAR. By optimizing the fabrication process we have successfully eliminated silicon grass in subsequently fabricated sensor prototypes.

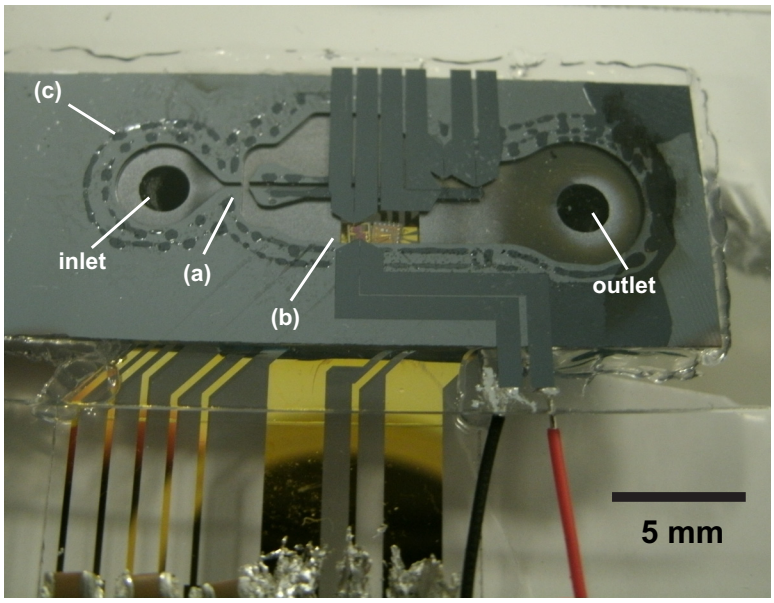

Figure 14: Photograph of a fabricated prototype of the MEMS air-microfluidic PM sensor.

5. Experimental Setup

Two fabricated prototypes of the air-microfluidic MEMS PM sensor (referred to as prototype A and B) were tested in a 25 m^3 air-quality test chamber at the Environmental Energy Technologies Division (EETD) of the Lawrence Berkeley National Laboratory. The microfluidic circuits of the two prototypes are identical; the only difference is the design of the thermophoretic heater, as shown on Figures 10a and 10b. These differences should have little effect on the sensitivity of the sensor, as both heaters

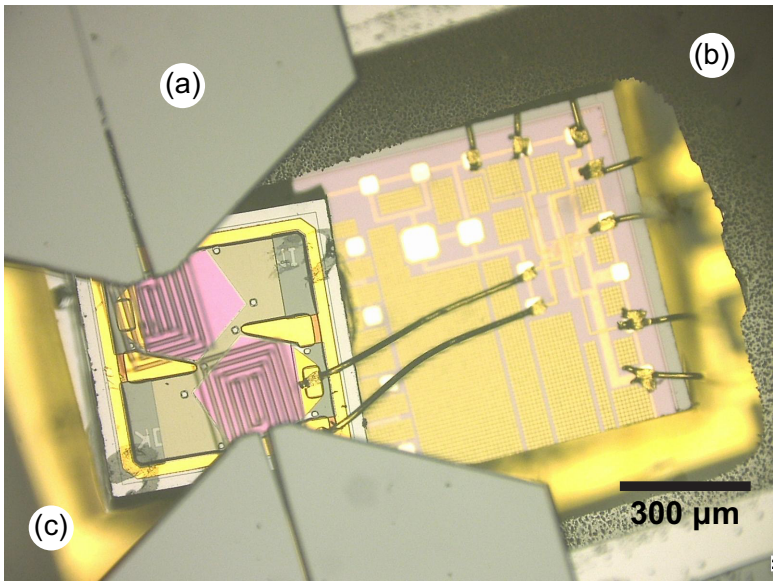

Figure 15: Optical micrograph of the area of the thermophoretic deposition, showing the alignment of all the three wafers ((a)-top wafer, (b)-middle wafer, and (c)-bottom wafer) comprising the final MEMS PM sensor.

are adjusted to dissipate approximately the same power. The sensor prototypes were exposed to both tobacco smoke and diesel exhaust. To generate representative concentrations of tobacco smoke, a single cigarette was lit and smoked using a custom built machine. To generate diesel exhaust, a portable diesel generator was used. A high-efficiency particle air (HEPA) filter unit (Control Resources Systems Inc., 600L) was used to obtain dilution air to lower the concentration of particles during testing. A DustTrak^{TM} Aerosol Monitor 8520 (TSI Inc.) was used to provide a reference for particle concentrations in the test chamber. The DustTrak provides an indirect measurement of PM mass and has been shown to overestimate fine particle mass concentration [12, 31]. Therefore, the DustTrak was first calibrated relative to PM collected on filters with mass directly determined by gravimetric analysis [14]. The output resonant frequency of the FBAR was measured using a spectrum analyzer (Agilent 8562EC) and recorded using a laptop running a custom-developed LABVIEW (v. 10.0f2) program.

6. Experimental Results

Average recorded sensitivity coefficients in Hz/min of frequency change per $\mu g/m^3$ of particle concentration for both prototypes are shown in Table 1. Prototype A failed before it was exposed to diesel exhaust, hence the sensitivity coefficient for diesel exhaust for prototype A is unavailable. As previously mentioned, the effects of the different heater designs on sensor sensitivity should be similar due to the same power dissipation and area covered by the heaters. Correspondingly, we attribute the higher sensitivity of prototype A to manufacturing variability, such as partial obstruction of the flow path and leaks close to the outlet port of prototype B. The variability in the sensitivity of future senor prototypes can be minimized by optimizing the microfabrication process, while the remaining difference can be further removed through calibration of the individual sensors.

Table 1: Average recorded sensitivity coefficient (in Hz/min of frequency change per $\mu g/m^3$ of particle concentration) for PM sensors prototypes A and B. Standard deviation is depicted in parenthesis.

	Tobacco smoke	**Diesel exhaust**
Prototype A	5.76 (0.68)	NA
Prototype B	1.70 (0.22)	2.46 (0.23)

The response of the sensor prototypes to tobacco smoke (prototype A) and diesel exhaust (prototype B) during two representative experiments is shown in Figures 16 and 17. In both cases, rates of frequency change (right axis) are displayed scaled to match the reference concentration obtained from the DustTrak (left axis). The x-axis denotes time in minutes elapsed from the start of the experiment. The gray region highlights the time when PM is introduced into the chamber, either in the form of a lit cigarette (Figure 16) or channeled exhaust from the diesel generator (Figure 17). Steep declines in PM concentrations are due to clean filtered air through the HEPA filter used to dilute particle concentrations in the source aerosol. The red and black lines show the rate of frequency change obtained using 1 and 4 min integration times, respectively.

Note that the reduction in tobacco smoke concentration from 25 to 15 $\mu g/m^3$ around $t = 130$ min in Figure 16 is also apparent in the 4 min average data for prototype A. This suggests a low-end sensitivity below 10 $\mu g/m^3$ at 4 min integration time.

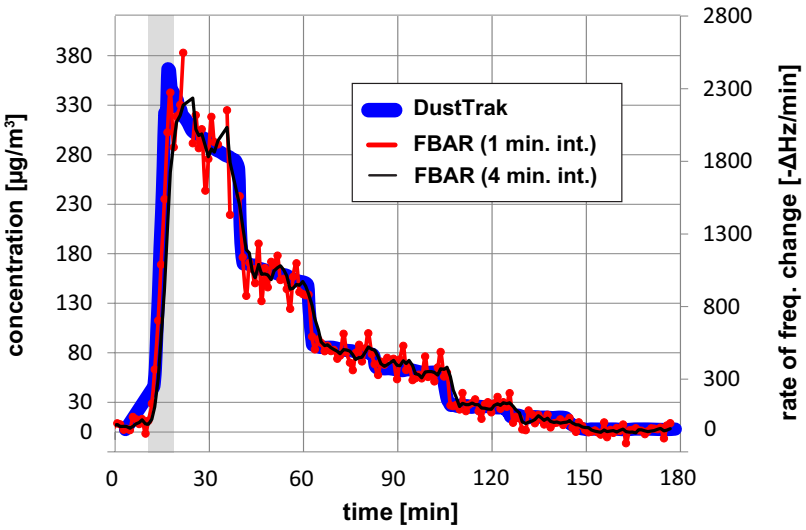

Figure 16: Data from a representative experiment showing the response of the sensor (prototype A) to tobacco smoke from a single lit cigarette. Steps in the curve represent addition of dilution air.

Based on the results from our experiments, we estimated the noise in the sensor signal to approach 50 Hz. This noise level was measured at low PM concentrations (i.e. below 50 μg/m^3). At high PM concentrations the noise is an artifact of the LabView recording method. This suggest a theoretical low-end detection limit of approximately 2 μg/m^3 at 10 min integration time.

Figures 18 and 19 show the average value of the sensitivity coefficient of prototype B for both tobacco smoke and diesel exhaust (respectively) while varying the flow rate through the microfluidic channel and the power to the thermophoretic heater. Low and high flow settings corresponds to 3 V and 4 V applied to the fan assembly, respectively, while low and high thermophoretic heater power corresponds to 14 and 18 V applied to the thermophoretic heater. The change in flow rate due to the change in fan voltage will affect the collection efficiency of the VI, however both diesel and tobacco smoke contain particles that are well below the 2.5 μm cutpoint, thus negating any impact the VI cutpoint has on the sensitivity data. The error bars represent the standard deviation for three 4 min integration time measurements.

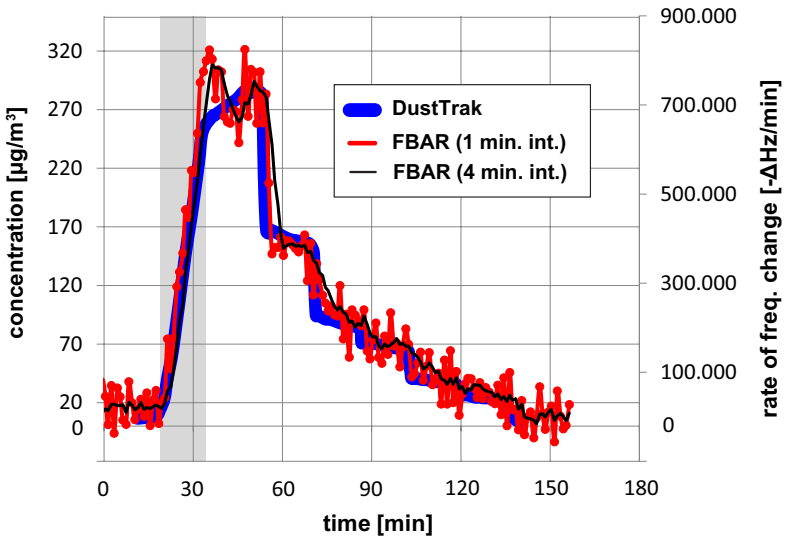

Figure 17: Data from a representative experiment showing the response of the sensor (prototype B) to diesel exhaust from a diesel generator. Steps in the curve represent addition of dilution air.

The results in Figures 18 and 19 show that the sensitivity of the MEMS PM sensor is strongly dependent on the flow rate through the microfluidic circuit. Higher flow-rate implies higher sensitivity at high heat. This high dependency on the flow suggests that our sensor is removing most particles from the air-stream in the microfluidic channel. Further more, it is interesting to observe that the sensitivity actually decreases with increased heater settings at the lower flow-rate in the case of diesel exhaust (Figure 19). This could be attributed to loss of particles by deposition *in front* of the active FBAR surface, such that fewer particles are deposited on the FBAR membrane. At higher flow-rates this effect is reduced likely because not all particles are removed from the airstream above the FBAR.

An optical micrograph of the surface of the FBAR (prototype A) with deposited particles is shown in Figure 20. A localized area of deposition, defined by the geometry of the thermophoretic heater, is clearly visible. The striped outline indicates the area on the FBAR, which was placed directly underneath the thermophoretic heater, while the direction of the airflow is indicated by the white arrow. The deposited particles form a crescent on the surface of the FBAR, further corroborating the theory of fully removing all

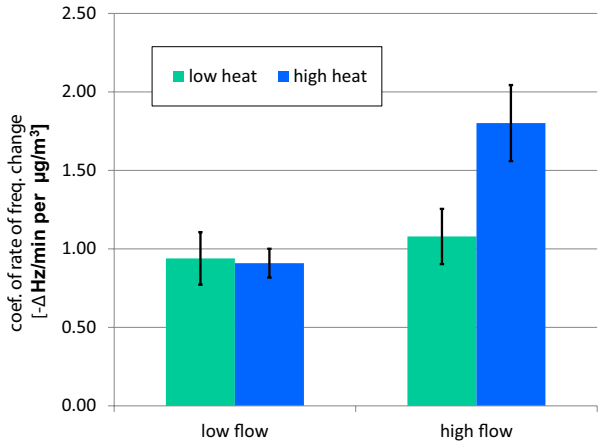

Figure 18: Recoded sensitivity coefficients for sensor prototype B while exposed to tobacco smoke under low and high flow rate and low and high power applied to the thermophoretic heater.

particles from the airstream above the FBAR. The particle-free spot at the far right underneath the heater suggests that particles are not deposited at that point.

7. Conclusions

Atmospheric particulate matter (PM) presents a significant health risk, and there is great need for a portable PM monitor that is capable of recoding and tracking personalized PM exposure. In this work we presented the design and fabrication of the MEMS air-microfluidic PM sensor and experimental results obtained from exposing the sensor to tobacco smoke and diesel exhaust, two commonly occurring PM sources. Our PM sensor is two orders of magnitude smaller than commercially available direct reading PM mass sensors; its small size enables its use in a portable personal PM monitoring application. Such application could be equipped with a cellular radio (for example connected to a cellphone) and GPS for geographically tagging the measured PM data and transmitting it to a central repository. The experimental results have shown that our sensor prototypes have sensitivity of approximately 2

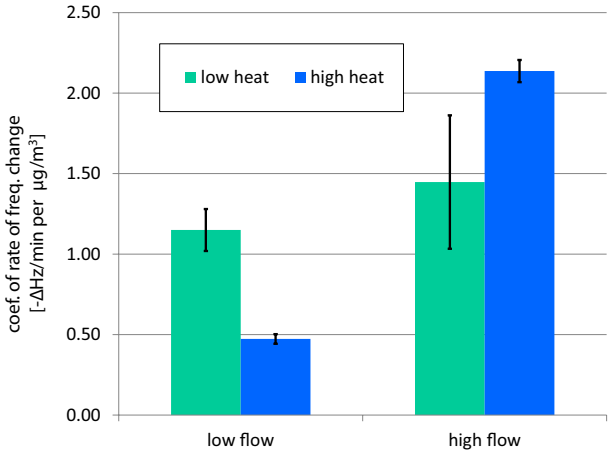

Figure 19: Recorded sensitivity coefficients for sensor prototype B while exposed to diesel exhaust under low and high flow rate and low and high power applied to the thermophoretic heater.

μg/m^3 with up to 10 min integration time. The experimental results indicate that the sensitivity of our sensors can be further increased by increasing the flow through the microfluidic channel, something that will be investigated in a future version of our MEMS PM sensor. Furthermore, the effect of external environmental factors such as temperature and humidity on the sensitivity of our sensor should be investigated. We envision future devices to contain microfabricated temperature and relative humidity sensors located inside the microfluidic channels in close proximity to the mass-sensing FBAR in order to accurately compensate for these effects.

Currently, data from our sensor is recorded using a computer-controlled spectrum analyzer and tracked with a Labview program. Designated electronic circuits for tracking the resonant frequency of the FBAR (such as presented in [32]) would help to reduce the measurement noise and to further increase the sensitivity of the sensor. Use of such a stand-alone electronic platform is also necessary to enable portable personal PM monitoring applications. We are currently working with several collaborators to develop the electronic platform and the connection to a cellular radio for enabling a self-contained portable PM sensing platform.

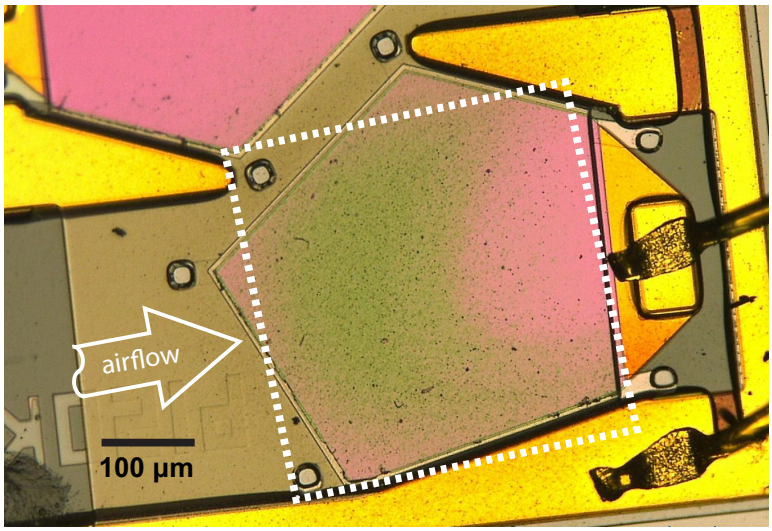

Figure 20: Optical micrograph of the surface of an FBAR after several deposition experiments (prototype A). Clearly visible is the crescent of deposited PM. During experiments, the airflow across the FBAR was from the left, as indicated by the arrow. The dashed outline indicates the FBAR area located directly beneath the thermophoretic heater.

The device presented in this work constitutes a simple air-microfluidic lab-on-a-chip for air quality measurements. Sensors of this type will allow for the collection of air quality exposure and source impact data that policy makers can use to obtain more accurate exposure assessments and linking of health effects to sources, as well as source impacts needed to develop more cost effective and efficient emissions control strategies.

8. Acknowledgements

The authors gratefully acknowledge Intel Corp., Qualcomm, and Aclima Inc. for their generous financial support of this work. We would like to acknowledge Justin Black for his initial work on this project. The microfabrication tasks was performed at the Marvel Nanofabrication Laboratory at UC Berkeley. The authors would like to thank Doug Sullivan from EETD for help in testing the sensor prototype, as well as Allison Woodruff and Alan Mainwaring from Intel Corp. for their supportive comments and technical discussion. Finally, we would like to acknowledge the support of Rich Ruby and Avago Technologies Inc. for providing high quality FBARs for our sensors, as well as for stimulating discussion. The U.S. Department of

Energy Commercialization Fund supported evaluation of the PM monitor in the environmental chambers of the Indoor Environment Group of the Energy Technologies Division of Lawrence Berkeley National Laboratory.

The U.S. Environmental Protection Agency through its Office of Research and Development assisted in the preparation of this article. It has been subjected to Agency's administrative review and approved for publication. Mention of trade names or commercial products does not constitute endorsement or recommendation for use.

References

[1] P. A. Solomon, P. Gehr, D. H. Bennett, R. F. Phalen, L. B. Mendez, B. Rothen-Rutishauser, M. Clift, C. Brandenberger, C. Muhlfeld, Macroscopic to microscopic scales of particle dosimetry: from source to fate in the body, Air Quality, Athmosphere and Health 5 (2012) 169–187.

[2] D. Krewski, Evaluating the effects of ambient air pollution on life expectancy, The New England Journal of Medicine 360 (4) (2009) 413–415.

[3] M. Kampa, E. Castanas, Human health effects of air pollution., Environmental Pollution 151 (2) (2008) 362–367.

[4] C. A. Pope, D. W. Dockery, Health effects of fine particulate air pollution: Lines that connect, Journal of the Air and Waste Management Association 56 (6) (2006) 709–742.

[5] National ambient air quality standards for particulate matter: Final rule., Part 50 available online at http://www.epa.gov/ttn/amtic/40cfr50.html, downloaded 23 July 2012., 40 CFR Parts 50, 43, and 58. Fed. Regist. 2006, 62 (138), U.S. Environmental Protection Agency, Office of Air Quality Planning and Standards: Research Triangle Park, NC (2006).

[6] BPA Air Quality Solutions LLC, Handheld Laser Particle Counter Reviews and Comparison, avaliable online: http://www.breathepureair.com/laser_particle_counters_handheld.html, downloaded on 11/24/2012.

[7] TSI Inc., DUSTTRAK DRX Aerosol Monitor 8534, avaliable online: http://www.tsi.com/DUSTTRAK-DRX-Aerosol-Monitor-8534/, downloaded on 11/24/12.

[8] J. Black, A. Elium, R. White, M. Apte, L. Gundel, R. Cambie, MEMS-enabled miniaturized particulate matter monitor employing 1.6 ghz aluminium nitride thin-film bulk acoustic wave resonator (fbar) and thermophoretic precipitator, in: the Proceedings of IEEE Ultrasonics Symposium, 2007, pp. 476–479.

[9] F. Doering, I. Paprotny, R. White, MEMS air-microfluidic sensor for portable monitoring of airborne particulates, in: the Technical Digest of the 15th Solid-State Sensor and Actuator Workshop, 2012, pp. 315–319.

[10] F. Fehsenfeld, D. Hastie, C. Chow, P. A. Solomon, Particulate Matter Science for Policy Makers: A NARSTO Assessment, Cambridge University Press, United Kingdom,, 2004, Ch. Chapter 5, Gas and Particle Measurements, pp. 159–189.

[11] P. H. McMurry, A review of atmospheric aerosol measurements, Atmospheric Environment 34 (2002) 1959–1999.

[12] J. C. Chow, P. Doraiswamy, J. G. Watson, L.-W. Chen, S. S. H. Ho, D. A. Sodeman, Advances in integrated and continuous measurements for particle mass and chemical composition, Journal of Air and Waste Management Association 58 (2008) 141–163.

[13] P. A. Solomon, C. Sioutas, Continuous and semicontinuous monitoring techniques for particulate matter mass and chemical components: A synthesis of findings from EPA's particulate matter supersites program and related studies, Journal of Air and Waste management Association 58 (2) (2008) 164–195.

[14] W. C. Hinds, Aerosol Technology: Properties, Behavior, and Measurement of Airborne Particles, 2nd Edition, John Wiley and Sons, 1999.

[15] T.-C. Hsiao, D.-R. Chen, S. Son, Development of mini-cyclones as the size-selective inlet of miniature particle detectors, Journal of Aerosol Science 20 (2009) 481–491.

[16] Y.-H. Kim, J.-Y. Maeng, D. Park, I.-H. Jung, J. Hwang, Y. J. Kim, Micromachined cascade virtual impactor with a flow rate distributor for wide range airborne particle classification, Applied Physics Letters 91 (043512) (2007) 1–3.

[17] I. Paprotny, F. Doering, R. M. White, Particulate matter (PM) monitor for cellular deployment, in: the Proceedings of the 9th Annual IEEE Conference on Sensors, 2010, pp. 2435–2440.

[18] P. Lawless, J. Thornburg, C. Rhodes, A. Vette, R. Williams, Personal exposure monitoring wearing protocol compliance: an initial assessement of quantitative measurements, Journal fo Exposure Science and Environmental Epidemilogy 22 (2012) 274–280.

[19] S. J. Lee, P. Demokritou, P. Koutrakis, J. M. Delgado-Saborit, Development and evaluation of personal respirable particulate samples (PRPS), Atmospheric Environment 40 (2) (2006) 212–224.

[20] W. Koch, W. Dunkhorst, H. Lodding, Design and performance of a new personal aerosol monitor, Aerosol Science and Technology 31 (2-3) (1999) 231–246.

[21] P. Demokritou, I. G. Kavouras, S. T. Ferguson, P. Koutrakis, Development and laboratory performance evaluation of a personal multipollutant sampler for simultaneous measurements of particulate and gaseous pollutants, Aerosol Science and Technology 35 (3) (2001) 741–752.

[22] R. M. White, I. Paprotny, F. Doering, W. E. Cascio, P. Solomon, L. A. Gundel, Sensors and apps for community-based atmospheric monitoring, Air and Waste Management Association Environmental Managers Magazine (2012) 36–40.

[23] COMSOL 4.3 release highlights, Tech. rep., COMSOL, avaliable online: http://www.comsol.com/products/4.3/#particletracing, downloaded on 12/11/2012 (May 17th 2012).

[24] J. R. Brock, On the theory of thermal forces acting on aerosol particles, Journal of Colloid Science 17 (1962) 768–780.

[25] J. P. Black, MEMS-based system for particle exposure assessement using thin-film bulk acoustic wave resonators and ir/uv optical discrimination, Ph.D. thesis, University of California, Berkeley (2006).

[26] J. Rosenbaum, Bulk Acoustic Wave Theory and Devices, Artch House, Inc., Norwood, MA, 1988.

[27] S. D. Senturia, Microsystem Design, Springer Science and Bussines Media, LLC, 2001.

[28] G. W. Pierce, Piezoelectric crystal resonators and crystal oscillators applied to the precision calibration of wavemeters, Proceedings of the American Academy of Arts and Sciences 59 (4) (1923) 81–106.

[29] R. Cerda, Pierce-gate crystal oscillator, an introduction, available online: http://www.crystek.com/documents/appnotes/pierce-gateintroduction.pdf, downloaded on 12/08/2012, Crystek Corporation (March 2008).

[30] P. K. Wright, D. A. Dornfeld, A. Chen, C. C. Ho, J. W. Evans, Dispenser printing for prototyping microscale devices, Transactions of NAMRI/SME 38 (2010) 555–561.

[31] S. Liu, Y. Zhu, A case study of exposure to ultrafine particles from secondhand tobacco smoke in an automobile, Indoor Air 20 (2010) 412–423.

[32] I. Paprotny, F. Doering, M. Seidel, R. White, M. Sokolov, A. Umnov, Fabrication of a miniaturized MEMS particular matter (PM) monitor, in: the Proceedings of the 10th Annual IEEE Conference on Sensors (IEEE SENSORS 2011), 2011, p. (open poster).